Alexandria Engineering Journal 89 (2024) 110–124

Contents lists available at ScienceDirect

Alexandria Engineering Journal

journal homepage: www.elsevier.com/locate/aej

Original article

Magnetohydrodynamic free convection of nano-encapsulated phase change materials between two square cylinders: Mapping the thermal behavior using neural networks

Mohammad Ghalambaz [a], Talal Yusaf [a,b], Ioan Pop [c,*], Jana Shafi [d], Manuel Baro [e,1], Mehdi Fteiti [f]

[a] College of Engineering, Almaaqal University, Basra 61003, Iraq
[b] School of Engineering and Technologies, Central Queensland University, Rockhampton, QLD 4701, Australia
[c] Department of Mathematics, Babeş-Bolyai University, 400084 Cluj-Napoca, Romania
[d] Department of Computer engineering and information, College of Engineering in Wadi Alddawasir, Prince Sattam bin Abdulaziz University, Saudi Arabia
[e] Researcher at the Tecnológico Nacional de México Campus Nuevo Casas Grandes, Nuevo Casas Grandes, Chih., Mexico
[f] Physics Department, Faculty of Science, Umm Al-Qura University, Makkah 24381, Saudi Arabia

ARTICLE INFO

Keywords:
Heat transfer enhancement
Nano encapsulated phase change material suspension
Natural convection
Phase change nanoparticles cores

ABSTRACT

The study focused on investigating the convective heat transfer of nano-encapsulated phase change suspensions in the presence of a non-uniform magnetic field within an annuli space between two square cylinders. The principal equations for the fluid flow and phase change heat transfer were formulated as partial differential equations and then represented into dimensionless format. The finite element method was used to solve these equations and simulate the free convection heat transfer. The effect of various factors, including Hartmann, Rayleigh, Eckert and Stefan numbers, geometry aspect ratio, nanoparticles' concentration, and fusion temperature, on the heat transfer rate was examined. A neural network was also introduced and trained to establish the connection between the control parameters (inputs) and the heat transfer rate (output). The outcomes were presented in the form of the modified Nusselt number, along with isotherms, heat capacity ratio (phase change) contours, and streamlines. The results demonstrated that the neural network could accurately predict the heat transfer rate and provide a comprehensive map of heat transfer with respect to the control parameters. Nano-Encapsulated Phase Change Materials (NEPCMs) can be considered as a new type of nanofluids, in which the nanoparticle consists of a core and a shell. The core part is made of a Phase Change Material (PCM) which can undergo solid-liquid phase change at a certain fusion temperature, and absorb/release a significant amount of energy due to latent heat of the phase change.

μ dynamic viscosity (kg/m)
ν kinematic viscosity, $(m^2 \bullet s^{-1})$
ρ fluid density, $(kg \bullet m^{-3})$
ρ_{sh} density of the particle's shell $(kg \bullet m^{-3})$
ρ_{c0} density of the core $(kg \bullet m^{-3})$
σ electrical conductivity $(\Omega.m)^{-1}$
θ dimensionless temperature
ω rotational (s^{-1})

Subscripts
f nanofluid; hybrid nanofluids
s solid phase

1. Introduction

The exploration of heat transfer phenomena has garnered substantial attention owing to its diverse applications across numerous domains, including energy, electronics, and manufacturing. Among the different modes of heat transfer, free convection plays a crucial role in many natural and industrial processes [1]. In an original paper by Ghalambaz et al. [2] has been stated that PCMs and nano-enhanced PCMs have been the subject of various engineering applications, particularly for thermal management systems and thermal energy storage applications. For instance, PCMs have been utilized for thermal management of buildings as a part of walls and roofs, windows as transparent building elements,

* Corresponding author.
E-mail address: ipop@math.ubbcluj.ro (I. Pop).
[1] ORCID: https://orcid.org/0000-0003-1665-8379

https://doi.org/10.1016/j.aej.2024.01.035
Received 15 July 2023; Received in revised form 23 October 2023; Accepted 8 January 2024
Available online 24 January 2024

Nomenclature

C_p	specific heat at constant pressure $(KJ/kg\ K)$
$(\rho C_p)_b$	heat capacity of the working fluid
Ec	Eckert number
f	volume fraction
g	acceleration due to gravity, $(m.s^{-2})$
h	convective heat transfer coefficient
H	height of the cavity (m)
(H_x, H_y)	components of the magnetic field H
k	thermal conductibility (W/m.K)
k_b	thermal conductivity $(W/m.K)$
Nu_x	local Nusselt number
Pr	Prandtl number
Re	local Reynolds number
Sn	size number
Ste	Stefan number
T	fluid temperature, (K)
T_h	temperature of the hot left wall (K)
T_c	temperature of the cold right wall (K)
(u, v)	dimensional velocity component of the fluid along the $(x, y)-$ directions, $(m \bullet s^{-1})$
(U, V)	dimensionless velocity component of the fluid along (X, Y) − directions
(x, y)	dimensional Cartesian coordinates - (m)
(X, Y)	dimensionless Cartesian coordinates

Greek symbols

β	volumetric coefficient of thermal expansion, (K^{-1})
γ	magnetic strength
δT	temperature interval
κ	thermal conductivity

domestic heat pump and air-conditioning systems, and other applications including space instruments, electronic cooling devices, and the food industry. Although PCMs are capable of storing/releasing a tremendous amount of energy on phase change, they are inherently very weak in terms of heat transfer.

In the recent years, nanofluids have received much attention because they are potentially used as a thermophysical heat transfer fluid, cooling engine components in the automotive industry, their property to convert solar energy into thermal energy, and improving absorption and storage capacity in solar panels, building heating systems, solar drying devices, and many others. Choi in 1995 [3] at Argonne National Laboratory, USA, was the first researcher who gave life to this concept of nanofluids. It is well known that mixing nanoparticle in a fluid involve a change in the liquid's thermophysical and optical properties such as thermal conductivity. But conventional (classical) viscous fluids do not allow to grow so efficiently the intensified fluid flow and heat transfer. In a paper by Alsabery et al. [4], a review on single and two-phase nanofluid models on the convection heat transfer in enclosures with inner bodies has been presented. Also, cconsiderable research efforts have been directed toward investigating the impact of various parameters on free convection heat transfer. Notably, the influence of enclosure shape [5,6] and the use of nanofluids in an open [7,8] or a confined space [4,9] has emerged as a significant area of interest. Interesting published papers on the present area are those by Mehrizi et al. [10,11], Graeilinezhad et al. [12], Hosseini et al. [13], and in the book by Merkin et al. [14].

The MHD effects on heat transfer have gained considerable attention due to their potential to manipulate fluid flow and heat transfer characteristics [15]. Under the influence of a magnetic field, the motion of electrically conducting fluids can be altered, leading to modified flow patterns and heat transfer rates [16]. In the context of natural convection, the application of MHD offers opportunities to control and improve convective heat transfer, making it an intriguing avenue for exploration [17]. Various aspects of heat transfer of nanofluids under the influence of magnetic fields have been investigated in recent years. For example, the triple diffusion of concentrations [18], nanofluids [19], and entropy generation [20] under a magnetic field have been explored. The magnetic field has also been used to control phase change in energy storage units [21].

Including nanoparticles in the base fluid alters its thermophysical properties, enhancing heat transfer characteristics. Nanoparticles exhibit high thermal conductivity and specific surface area, significantly enhancing convective heat transfer by promoting effective heat dissipation. Additionally, PCMs in the suspension allow heat storage through the latent heat of phase transition, contributing to the enhancement of heat transfer [2,22].

In recent years, nano-encapsulated phase change materials (NEPCMs) have emerged as promising approach to enhance heat transfer performance. NEPCMs offer high latent heat storage and improved thermal conductivity, which can significantly enhance the heat transfer rate [23,24]. Recent research has demonstrated the enhanced heat transfer characteristics of NEPCM slurries in various configurations, such as microchannels [23] and enclosures [25,26]. Furthermore, the preparation and thermal properties of NEPCMs have been extensively studied for their potential in thermal energy storage [27,28].

The free convection of nano-encapsulated phase change material (NEPCM) suspensions in enclosures under the influence of magnetic fields has not received sufficient attention in the existing literature, despite its significance. Previous studies have primarily concentrated on investigating free convection heat transfer in more straightforward geometries and without magnetic effects, including I shape [29], grooved [30], L shape [31], prismatic [32], crescent-shaped [33], rectangular [34], wavy wall [35,36], heated and cooled cylinders [37], or cavity containing fins [38]. As a result, there remains a noticeable gap in the research when it comes to exploring the mixed convection behavior of NEPCM suspensions within a lid-driven trapezoid cavity.

Fereidooni [39] studied the natural convection of NEPCMs within an L-shaped cavity, considering the influence of a uniform magnetic field. By employing the Finite Element Method (FEM) to solve the governing equations under specific boundary conditions, the effects of Rayleigh number, nanoparticle concentration, Stefan number, Hartmann number, and non-dimensional fusion temperature on temperature, velocity, streamline, heat capacity ratio, and average Nusselt number contours are examined. Findings indicate that raising the Hartmann number from 0 to 20 decreases the average Nusselt number by up to 17%, while higher nanoparticle concentrations enhance the Nusselt number by 26%.

NEPCM suspensions are an innovative nanomaterial solution. These mixtures comprising a host fluid and NEPCM particles can circulate across heated or chilled surfaces. The phase change nanoparticles embedded within significantly enhance heat transfer, harnessing their latent heat of fusion to modulate heat transfer rates or surface temperatures. A review of recent studies demonstrates a notable surge in interest regarding the heat transfer capabilities of NEPCM suspensions over the past two years, underlining their distinctive thermal properties. Despite this, many facets of these groundbreaking nanomaterials, such as the impact of a non-uniform magnetic field on their convection heat transfer, remain uncharted territory. Consequently, this study's primary objective is to delve into the effects of a non-uniform magnetic field on the free convection of NEPCM suspensions within the context of the space between two square cylinders for the first time. It is shown that the fusion temperature of the nano-encapsulated phase change material

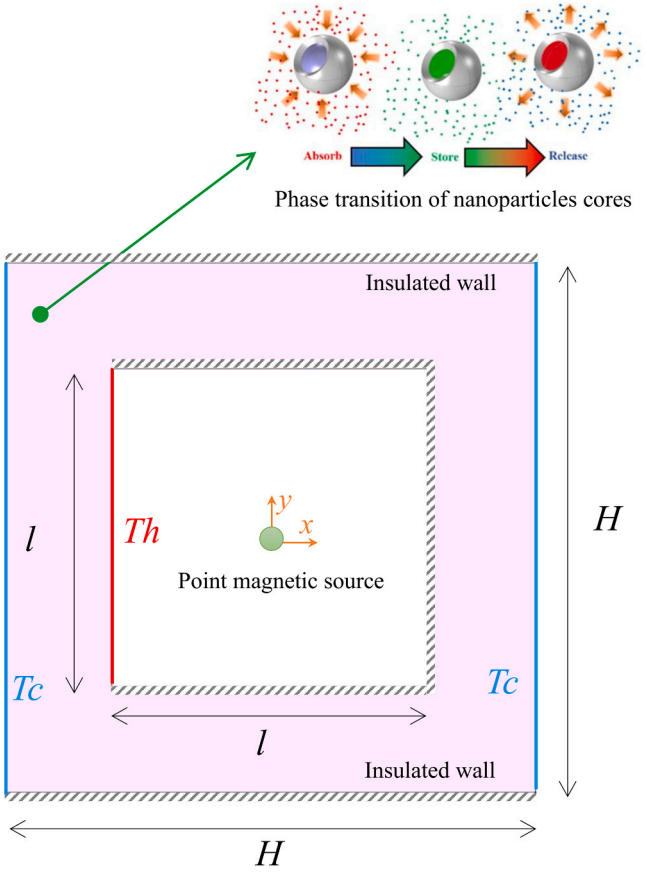

Fig. 1. Physical model and the simulation domain.

(NEPCM) and the Hartmann number significantly affected the Nusselt number. The highest Nusselt number was observed at a fusion temperature of 0.4 for all Hartmann numbers when the enclosure aspect ratio was 0.6. The fusion temperature and NEPCM concentration also substantially impacted the heat transfer rate. An increase in nanoparticle concentration enhanced the influence of fusion temperature on heat transfer, with the highest rate observed at a fusion temperature of 0.4. Changing the fusion temperature from 0.1 to 0.4 resulted in a 4% improvement in heat transfer for a nanoparticle concentration of 0.05, emphasizing the importance of fusion temperature in enhancing heat transfer performance. Additionally, by adding NEPCM particles, overall heat transfer improves significantly, with an approximate 38% increase. The results of the paper are original and have not been published by any researcher.

2. Physical model

The heat transfer occurring within a cavity channel, as illustrated in Fig. 1, is modeled in the following manner, where H is the height of the cavity and l is distance between two square cylinders. The region between the two cylinders is occupied by a suspension of NEPCM particles in water. The heated surface within the system corresponds to a heat-generating element, such as electrical components or vapor condensation. In the context of evaporative cooling for electronic components, substances like FC-72 [40] are commonly used. These liquids facilitate heat dissipation from the electronic components, contributing to effective cooling in the system. On the other hand, the cold walls serve the purpose of cooling the system either through heat dissipation to the surroundings or by utilizing radiators.

The nanoparticles possess a core made of PCM, enabling them to undergo a phase change while being suspended in the water. Consequently, the nanoparticles not only modify the thermophysical properties of the nanofluid (NEPCM-water), such as thermal conductivity and dynamic viscosity, but also locally affect the heat capacity. This heat capacity is dependent on temperature and is directly influenced by the phase transition temperature of the PCM nanoparticle cores, denoted as T_f. The temperature-dependent characteristics of the nanoparticles contribute to unique cooling and energy storage capabilities.

In Fig. 1, a phase change phenomenon of a nanoparticle's core within water is illustrated. The core of the nanoparticle can exist in various states, including solid, liquid, or undergoing a phase transition, as it moves through the water. Specifically, the model considers a configuration where the sidewalls of the channel are fixed at a low temperature, T_c with $(T_c < T_f)$, while the sidewall of the inner duct is preserved at a high temperature, T_f with $(T_h > T_f)$. The NEPCM water, serving as the working fluid, absorbs heat adjacent to the hot wall and melts the nanoparticles' cores. Subsequently, the working fluid, consisting of water and NEPCM particles with molten cores, rises due to buoyancy effects and reaches the top wall, which is well insulated. The flow continues its path until it reaches the right cold wall, where the nanoparticles undergo a phase transition, releasing their latent heat to the cold wall and solidifying. The cold and dense working fluid, along with solidified nanoparticles' cores, descends and reaches the bottom wall before moving towards the left heated wall, thereby continuing the cycle. There is a magnetic source term at the center of the channel, as depicted in Fig. 1. In order to express the magnetic field strength, it is assumed that the magnetic source corresponds to a vertically positioned magnetic wire at the center of the coordinate system within the $(x-y)$ plane. The magnetic field components (H_x, H_y) and the magnetic field strength (H) can be represented as [41,42]:

$$H_x^* = \frac{\gamma}{2\pi}\left(\frac{1}{x^2+y^2}\right)y, H_y^* = -\frac{\gamma}{2\pi}\left(\frac{1}{x^2+y^2}\right)x \quad (1)$$

where $H^* = \sqrt{H_x^{*2} + H_y^{*2}}$ and γ denotes the magnetic strength.

Due to their minuscule dimensions, the encapsulated particles lack substantial temperature variations internally, rendering them appropriate for implementing nanoparticles and phase change in lamp models. Table 1 provides a comprehensive overview of the crucial characteristics of the core, host fluid, and shell. It is worth mentioning that the core of the NEPCM exhibits a fusion temperature of around 32 °C, along with a latent heat of 211 kJ/kg [43].

Under the current configuration, both water and particles are considered to be incompressible. The working fluid is assumed to be Newtonian and exhibits laminar flow. The Bosinesque model is employed to account for the buoyancy forces in the system. Considering these assumptions, the next section provides the mathematical equations to express the natural convection heat transfer of NEPCM-water suspension in the enclosure.

Table 1
Properties of the shell material (*PU*), the host fluid and core material (nonadecane) of NEPCM particles [43–45].

	k	ρ	Cp	μ	σ	β
PU	—	786	1317.7	—	10^{-6}	17.28×10^{-5}
Host fluid	0.613	997.1	4179	8.9×10^{-4}	0.05	21×10^{-5}
Nonadecane	—	721	2037	—	—	—

Table 2
The utilized equations for computing the properties of NEPCM suspension.

Property	Ref.	Formula Eq.	
Mixture density	[2,47]	$\rho_b = (1-f)\rho_f + f\rho_p$	(5)
NEPCM particles density	[2,47]	$\rho_p = (1+\iota)(\rho_{co}\rho_{sh})(\rho_{sh}+\iota\rho_{co})^{-1}$	(6)
Mixture specific heat capacity	[48,49]	$C_{p,b} = \rho_b^{-1}(\rho_f C_{p,f}(1-f) + \rho_p C_{p,p} f)$	(7)
Specific heat capacity NEPCM particle core	[2,47,50]	$C_{p,p} = C_{p,co} + \left\{\frac{\pi}{2}.\left(\frac{h_{sf}}{T_{Mr}} - C_{p,co}\right)\sin\left(\pi\frac{T-T_f+\delta T/2}{\delta T}\right)\right\}\zeta$ $\zeta = \{ \quad 0T < T_f - \delta T/2 \quad 1T_f - \delta T/2 < T < T_f + \delta T/2 \quad 0T > T_f + \delta T/2$	(8)
Mixture thermal expansion	[2,50]	$\beta_b = (1-f)\beta_f + f\beta_p$	(9)
Mixture thermal conductivity	[2,51,52]	$\frac{k_b}{k_f} = 1 + Nc\, f$	(10)
Mixture dynamic viscosity	[2,51,52]	$\frac{\mu_b}{\mu_f} = 1 + Nv\, f$	(11)
Mixture electrical conductivity	[41]	$\frac{\sigma_b}{\sigma_f} = 1 + \frac{3\left(\frac{\sigma_b}{\sigma_f}-1\right)f}{\left(\frac{\sigma_s}{\sigma_f}+2\right) - \left(\frac{\sigma_s}{\sigma_f}-1\right)f}$	(12)

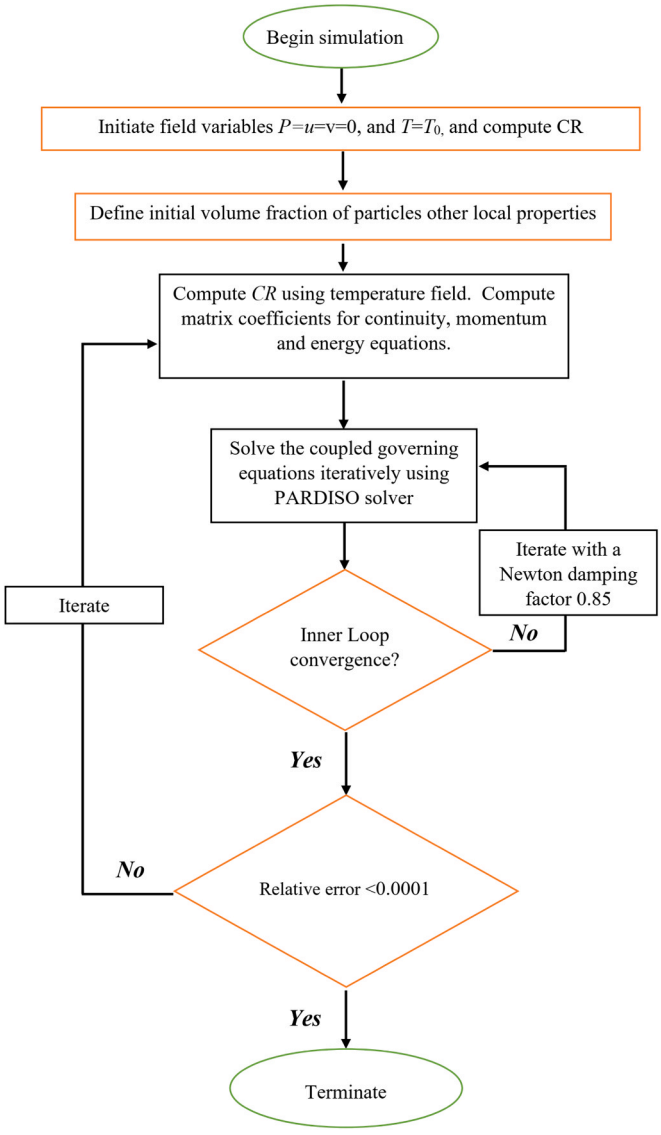

Fig. 2. A diagram of the applied solution method.

Table 3
Details of the mesh elements and the corresponding local *Nu* for examined meshes.

Sn	Free-quads	*Nu*	*Error %
0.015	2857	6.807	2.1
0.01375	3430	6.864	1.3
0.0125	4096	6.883	1.1
0.01125	5186	6.929	0.4
0.01	6400	6.956	-

* Error %= 100 × $|Nu\text{-}Nu_{@Sn=0.01}|/Nu_{@Sn=0.01}$

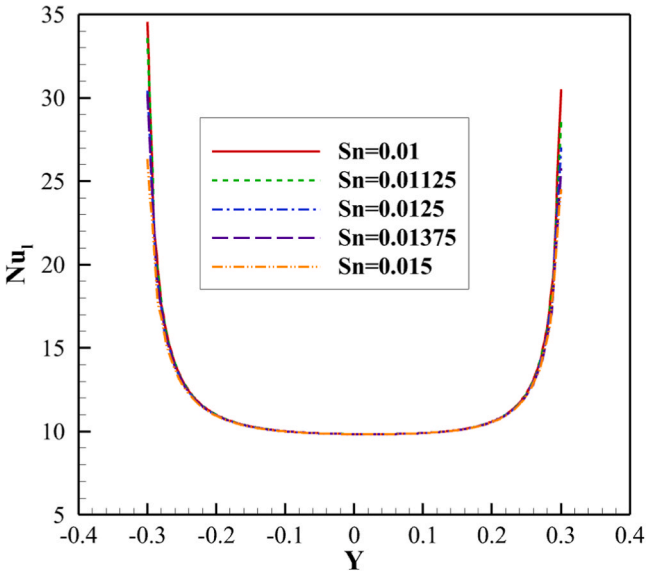

Fig. 3. Variation of the local Nusselt number with *Y* for various mesh sizes.

2.1. Model equations

The flow dynamics in this study are modeled by incorporating the continuity and momentum equations, following the approach outlined in reference [2]. Additionally, the influence of buoyancy forces is taken into account by considering a temperature-dependent body force. Furthermore, the impact of magnetic fields is included in the momentum equation through body force source terms, as elaborated in references

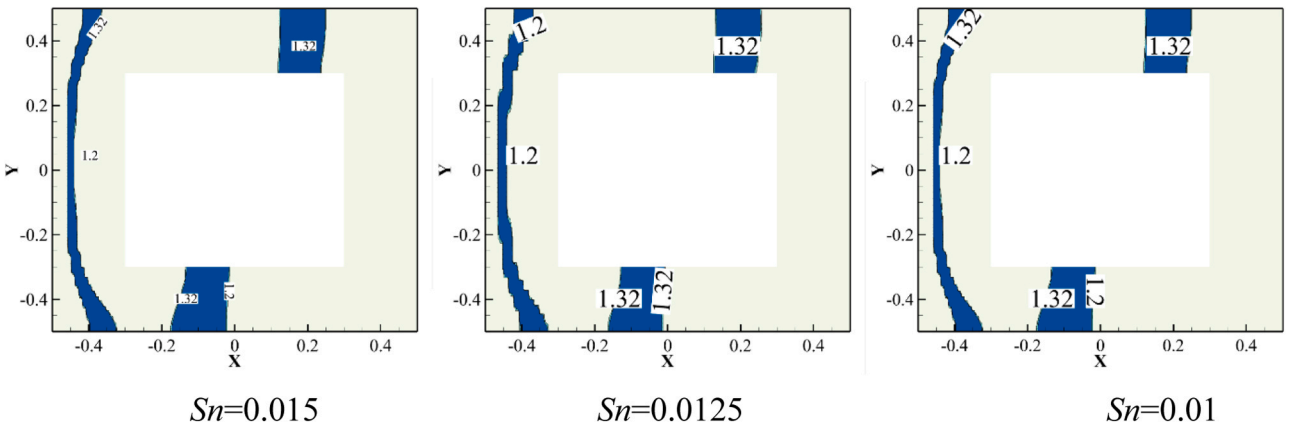

Fig. 4. The CR contour maps for various mesh sizes.

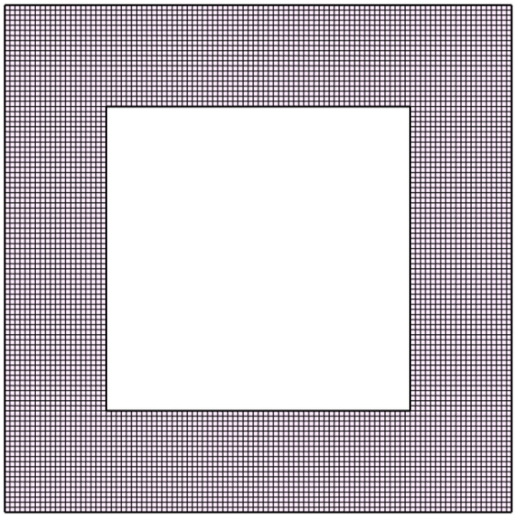

Fig. 5. A view of the selected grid adopted for the rest of the computations.

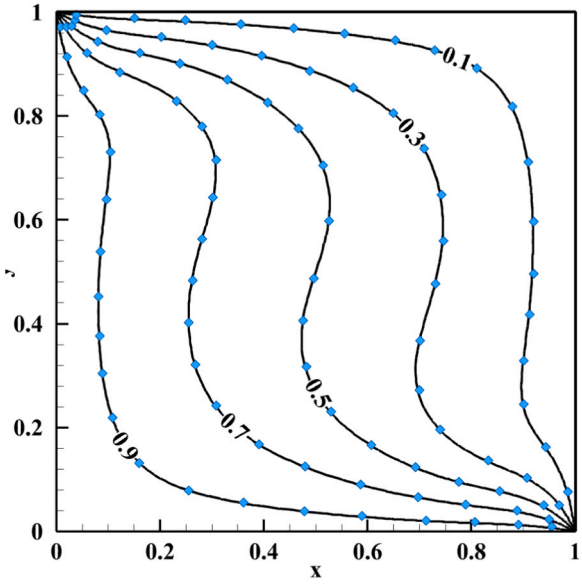

Fig. 6. Isotherms computed in [16] with Ha= 50, Ra= 10^5, and a magnetic angle of 90°: the results of the current research are plotted by solid lines, and symbols indicate the results of literature.

Table 4
Comparative analysis of average Nusselt number *Nu* between the current investigation and the work by Matin and Pop [62].

f	Matin and Pop[62]	Current simulations	Distance
0.01	5.66	5.63	0.53%
0.02	5.89	5.84	0.85%
0.03	6.02	6.1	1.33%

[41,46].

Continuity

$$\frac{\partial}{\partial x}\frac{u}{} + \frac{\partial}{\partial y}\frac{v}{} = 0 \tag{1}$$

Momentum in x and y directions:

$$\rho_b u\frac{\partial u}{\partial x} + \rho_b v\frac{\partial u}{\partial y} = -\frac{\partial p}{\partial x} + \mu_b\left(\frac{\partial^2 u}{\partial x^2} + \frac{\partial^2 u}{\partial y^2}\right) - \sigma_b B_y^2 u + \sigma_b B_x B_y v \tag{2}$$

$$\rho_b u\frac{\partial v}{\partial x} + \rho_b v\frac{\partial v}{\partial y} = -\frac{\partial p}{\partial y} + \mu_b\left(\frac{\partial^2 v}{\partial x^2} + \frac{\partial^2 v}{\partial y^2}\right) + g\rho_b\beta_b(T - T_c) + \sigma_b B_x B_y u - \sigma_b B_x^2 v \tag{3}$$

where the significance of $B_x = \mu_0 \quad H_x^*$, $B_y = \mu_0 H_y^*$, $u, v, p, T, g, \mu_b, \rho_b, \sigma_b$ and β_b are mentioned in the Nomenclature. The subscript *b* denotes the bulk NEPCM suspension as a uniform mixture. In the governing equations under consideration, a steady-state form has been utilized. This is owing to the phase change of nanoparticle cores, a process that transpires continuously within a distinct material space, and has been modeled via a lumped approach. As the suspension circulates throughout the enclosure, it maintains a perpetual state of phase transition. New NEPCM particles are ceaselessly introduced to the flow, where they engage with a particular material space within the domain, absorbing or releasing their latent heat before being carried off by the ongoing suspension stream. While this specific heat transfer phenomenon presents non-uniformity in flow, phase transition, and heat transfer across the material space, it maintains a consistent pace over time, thus rendering it suitable for steady-state analysis.

Energy conservation.

The energy conservation for the suspension includes a heat capacity term which depends on local temperature as [2]:

$$(\rho Cp)_b u\frac{\partial T}{\partial x} + (\rho Cp)_b v\frac{\partial T}{\partial y} = k_b\left(\frac{\partial^2 T}{\partial x^2} + \frac{\partial^2 T}{\partial y^2}\right) + \sigma_b\left(uB_y - vB_x\right) \tag{4}$$

The term $\sigma_b(uB_y - vB_x)$ represents the heat generation resulting from

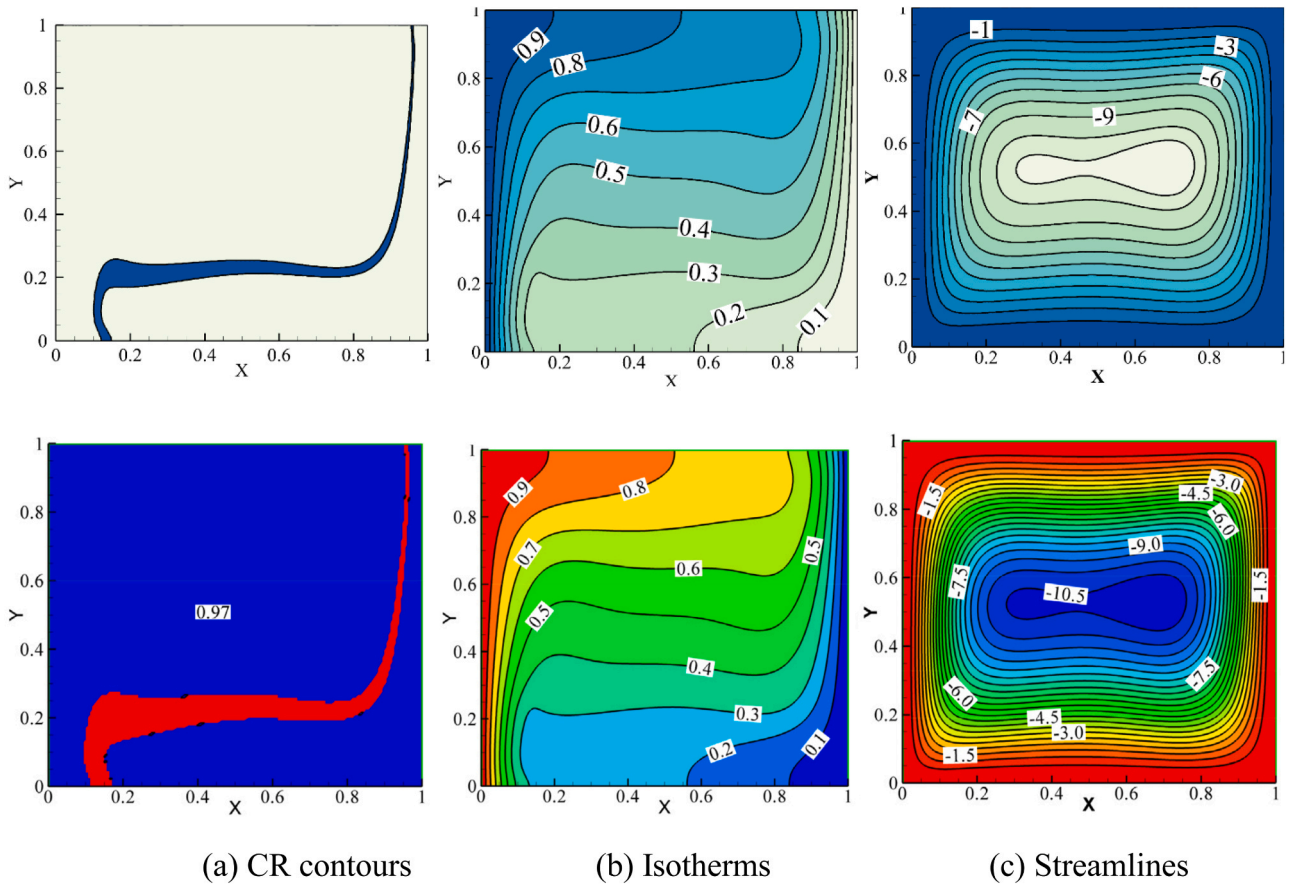

Fig. 7. Comparison between the CR, isotherms, and streamlines of the present study and those of [2] for heat transfer of NEPCM suspensions in a square cavity for $Ra = 10^5, \theta_f = 0.3, Pr = 6.2, Ste = 0.3, \kappa = 0.33, Nv = 12.5, Nc = 23.8, Ec = 0, Ha = 0, f = 0.05 and \frac{\rho_p}{\rho_f} = 0.9$.

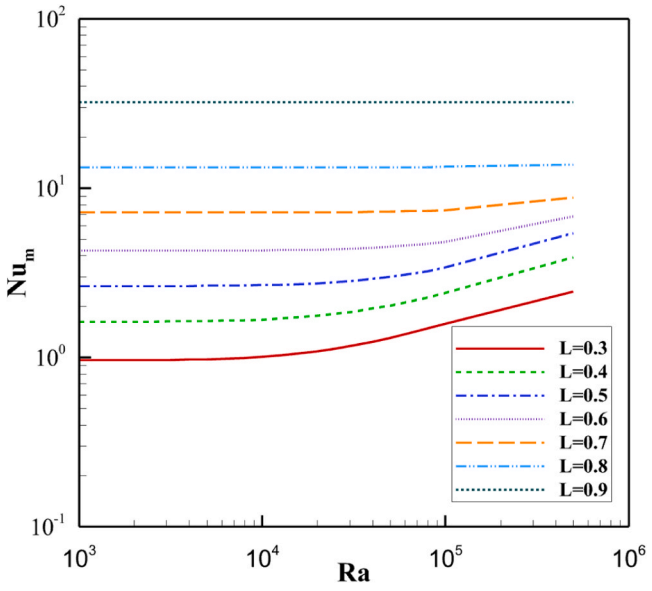

Fig. 8. Variation of the modified Nusselt number with *Ra* for various aspect ratio (*L*) values.

the presence of the magnetic field, as discussed in reference [41]. In this context, $(\rho C_p)_b$ refers to the heat capacity of the working fluid (NEPCM-water), which is dependent on the local temperature. Further elaboration on this term will be provided later. The heat transfer in the system is governed by Fourier's law of heat conduction, with a thermal conductivity denoted as k_b..

The boundary conditions applied in the simulation are as follows: The insulated walls, as shown in Fig. 1, have an applied boundary condition of $\partial T/\partial N = 0$ (the derivative of temperature with respect to the normal vector of the surface) equal to zero, indicating no heat transfer through those walls. The temperature at the hot wall is set to $T = T_h$, maintaining a constant isothermal condition. The temperature at the cold wall is set to $T = T_c$, maintaining a constant isothermal condition. The velocity of the fluid at all surfaces is set to zero $(u, v) = 0$ indicating no flow or movement of the fluid across the boundaries. At the bottom left corner, a reference pressure with zero-gauge pressure is applied. This establishes a reference point for pressure calculations in the system. These boundary conditions help define the thermal and fluid behavior within the computational domain.

2.2. The suspension as a bulk model

The NEPCM suspension is treated as a uniform mixture of NEPCM particles and host fluid (water) [2]. The effective thermophysical properties were utilized and calculated based on the data presented in Table 2.

The concentration of NEPCM particles is represented by the symbol f,. The core-shell weight ratio, denoted as l, has an approximate value of 0.447 [43]. The term δT is introduced to ensure continuity in the energy balance. Furthermore, h_{sf} corresponds to the latent heat of NEPCM particle cores.

The coefficients *Nc* and *Nv* in these equations represent the thermal conductivity and dynamic viscosity numbers, respectively. These coefficients are influenced by various factors such as nanoparticle type, size, host fluid type, temperature, and the method of nanofluid prepa-

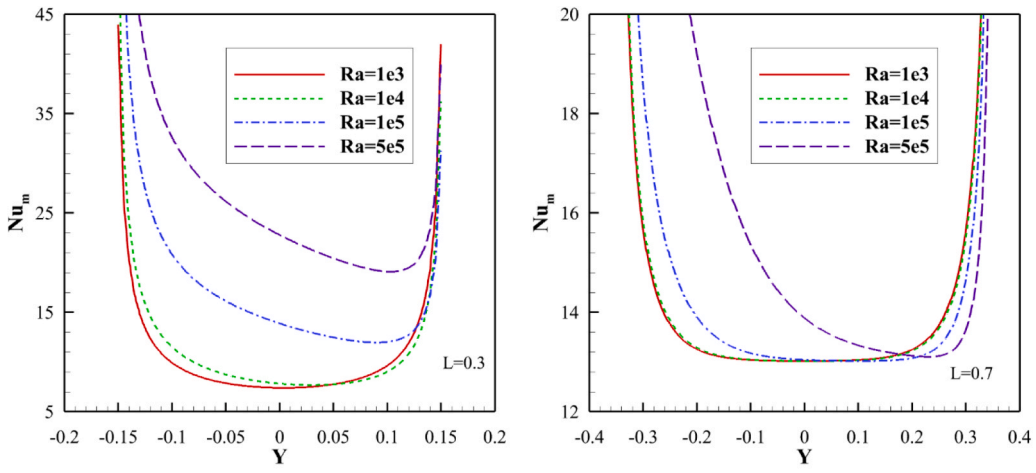

Fig. 9. Variation of the local Nusselt number with x for a range value of Ra and two cases of the aspect ratio (a) $L = 0.3$ and (b) $L = 0.7$..

ration [51,52]. However, in the case of a synthesized nanofluid, these coefficients can be assumed to be constant. These equations are applicable specifically for low nanoparticle volume fractions, f, specifically, when $f \leq 5\%$.

2.3. Dimensionless form of equations

In order to present a universal representation of the NEPCM suspension's behavior, the governing equations and their corresponding boundary conditions can be transformed into a dimensionless format. This involves introducing specific non-dimensional variables to facilitate this transformation.

$$X=\frac{x}{H},\quad Y=\frac{y}{H},\ L=\frac{l}{H},\ U=\frac{uH}{\alpha_f},\ V=\frac{vH}{\alpha_f},\quad P=\frac{pH^2}{\rho_f\alpha_f^2},\quad \theta=\frac{T-Tc}{Th-Tc},$$
$$\widetilde{H}=\frac{H^*}{H_0},\quad \widetilde{H}_x=\frac{H_x^*}{H_0},\ \widetilde{H}_y=\frac{H_y^*}{H_0},\ \theta_f=\frac{T_f-Tc}{(Th-Tc)} \tag{13}$$

where $H_0 = H^*(H/2,0) = \gamma/2\pi H$. After plugging in the dimensionless variables into the governing equations, a set of non-dimensional governing equations was derived:

$$\left[\frac{\partial U}{\partial X}+\frac{\partial V}{\partial Y}\right]=0 \tag{14}$$

$$\left(\frac{\rho_b}{\rho_f}\right)\left[U\frac{\partial U}{\partial X}+V\frac{\partial U}{\partial Y}\right]=\Pr\left(\frac{\mu_b}{\mu_f}\right)\left(\frac{\partial^2 U}{\partial Y^2}+\frac{\partial^2 U}{\partial X^2}\right)-\frac{\partial P}{\partial X}-$$
$$\mathrm{Ha}^2\Pr\left(\frac{\sigma_b}{\sigma_f}\right)\left(H_y^2U-H_xH_yV\right) \tag{15}$$

$$\left(\frac{\rho_b}{\rho_f}\right)\left[U\frac{\partial V}{\partial X}+V\frac{\partial V}{\partial Y}\right]=\Pr\left(\frac{\mu_b}{\mu_f}\right)\left(\frac{\partial^2 V}{\partial Y^2}+\frac{\partial^2 V}{\partial X^2}\right)-\frac{\partial P}{\partial Y}+$$
$$\mathrm{Ra}\times\Pr\left(\frac{\rho_b}{\rho_f}\right)\left(\frac{\beta_b}{\beta_f}\right)\theta-\mathrm{Ha}^2\Pr\left(\frac{\sigma_b}{\sigma_f}\right)\left(H_x^2V-H_xH_yU\right) \tag{16}$$

$$CR\left[U\frac{\partial\theta}{\partial X}+V\frac{\partial\theta}{\partial Y}\right]=\left(\frac{k_b}{k_f}\right)\left(\frac{\partial^2\theta}{\partial X^2}+\frac{\partial^2\theta}{\partial Y^2}\right)+\mathrm{Ha}^2\mathrm{Ec}\left(\frac{\sigma_b}{\sigma_f}\right)\left(UH_y-VH_x\right)^2 \tag{17}$$

The dimensionless parameters appeared in the above-written equations are Ra, Pr, Ha, Ec Ste and κ, defined in the Nomenclature, are given by,

$$\mathrm{Ra}=\frac{\rho_f g\beta_f(Th-Tc)H^3}{\alpha_f\mu_f},\ \Pr=\frac{\mu_f}{\rho_f\alpha_f},\quad Ha=\mu_0H_0L\sqrt{\frac{\sigma_f}{\mu_f}},$$
$$Ec=\frac{(\alpha\quad\mu)_f}{(\rho\quad C_p)_f\quad(T_h-T_c)\quad H^2},\ Ste=\frac{(\rho\quad C_p)_f\quad(T_h-T_c)\quad(\rho_{sh}+l\quad\rho_{c0})}{\alpha_f\quad(h_{sf}\quad\rho_{c0}\quad\rho_{sh})} \tag{18}$$
$$\kappa=\frac{(Cp_{c0}+l\quad Cp_{sh})\rho_{c0}\quad\rho_{sh}}{(\rho\quad C_p)_f\left(\rho_{sh}+l\quad\rho_{c0}\right)},$$

where

$$\left(\frac{\beta_b}{\beta_f}\right)=(1-f)+f\left(\frac{\beta_p}{\beta_f}\right),\left(\frac{\rho_b}{\rho_f}\right)=(1-f)+f\left(\frac{\rho_p}{\rho_f}\right) \tag{19}$$

Besides, $\delta=\delta T/(T_h-T_c)=0.05$ [2], in which δ is the non-dimensional phase change interval.

It is also assumed that the expansion of NEPCM particles is similar to that of the host fluid, resulting in approximate ratios of $(\beta_b/\beta_f)\sim 1$ and $(\rho_b/\rho_f)\sim 0.74$ [53]. Since the electrical conductivity of PU is minimal compared to water, its influence can be disregarded, leading to $(\sigma_s/\sigma_f)\sim 1$. Additionally, CR is defined as

$$CR=\frac{(\rho Cp)_b}{(\rho Cp)_f}=(1-f)+\frac{f}{\delta\times\mathrm{Ste}}\zeta+f\kappa \tag{20}$$

Furthermore, the non-dimensional fusion function (ς) was achieved as:

$$\zeta=\frac{\pi}{2}\times\ \sin\left(\frac{\pi}{\delta}\left(\theta-\theta_f+\delta/2\right)\right)\times\begin{cases}0\theta<\left(\theta_f-\delta/2\right)\\ 1\left(\theta_f-\dfrac{\delta}{2}\right)<\theta<\left(\theta_f+\delta/2\right)\\ 0\theta>\left(\theta_f+\delta/2\right)\end{cases} \tag{21}$$

The non-dimensional boundary conditions, are similar with the ones used by Sheremet et al. [54], namely, $\theta=1$, at the hot and $\theta=0$at the coled walls, $(U,V)=0$ at all walls, $\partial\theta/\partial N=0$, insulated boundary conditions at the upper and lower walls of the cavity, $P=0$, reference pressure at the point, were applied. The local $(Nu_l=h\,H/k_f)$ and average Nu Nusselt numbers at the bottom wall are considered key heat transfer parameters, and they can be defined as follows:

$$\mathrm{Nu}_l=-\left(\frac{k_b}{k_f}\right)\left(\frac{\partial\theta}{\partial N}\right)\Big|_{Hot\ wall}=-(1+Ncf)\left(\frac{\partial\theta}{\partial N}\right)\Big|_{Hot\ wall} \tag{22}$$

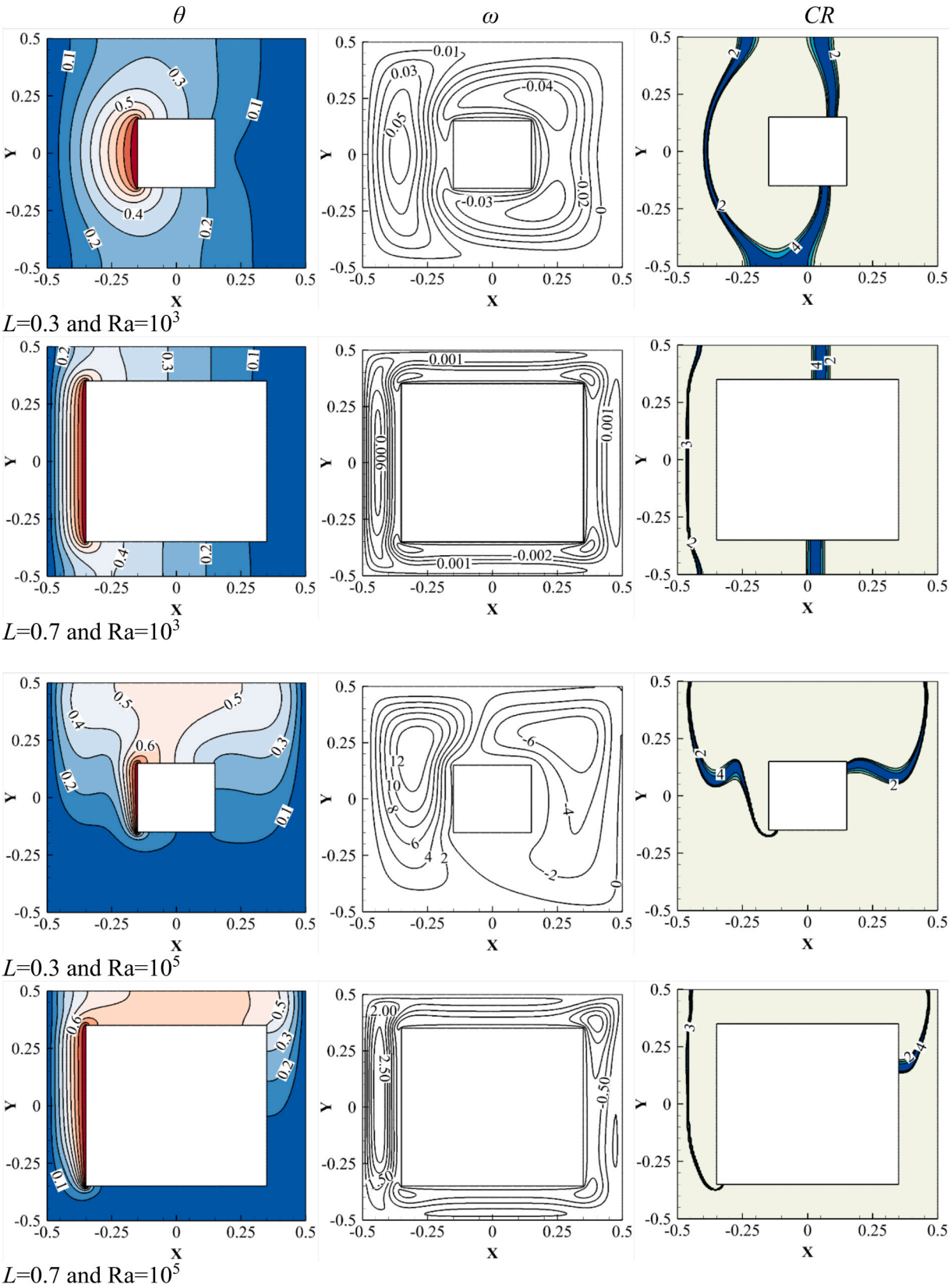

Fig. 10. A comparison of isotherms, streamlines, and CR contours for various *L* and *Ra*..

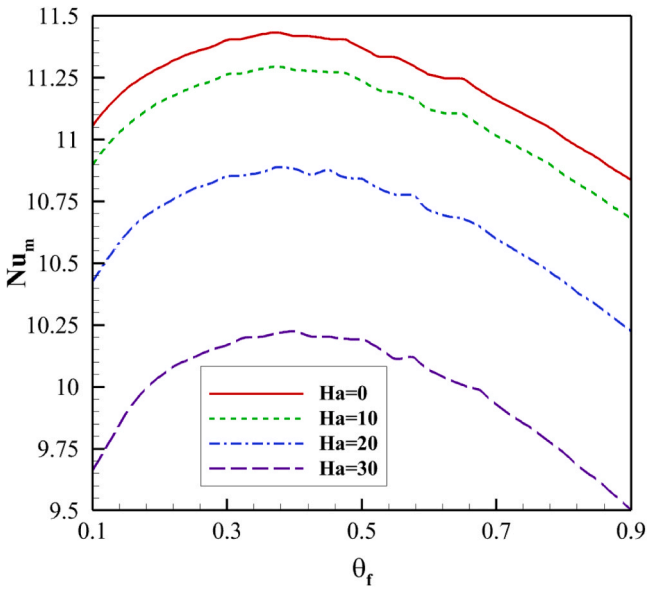

Fig. 11. Variation of modified Nusselt number for a range of fusion temperature (θ_f) and numerous Hartmann numbers when $L = 0.6$..

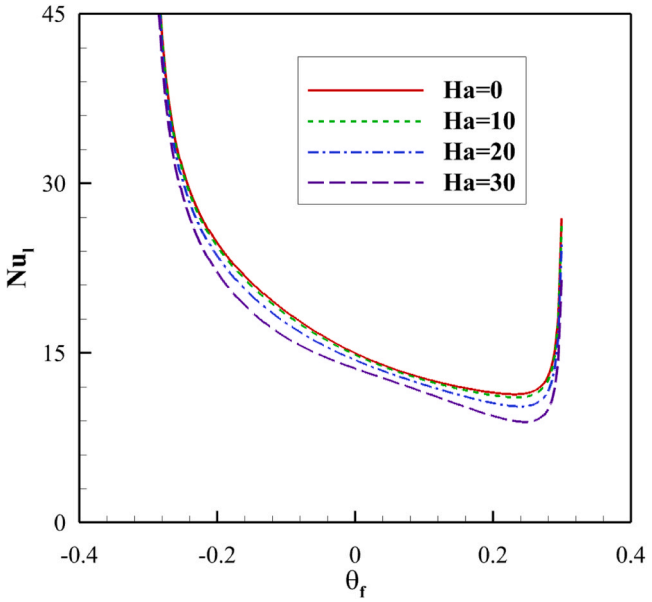

Fig. 12. Variation of the local Nusselt number with θ_f For various values of Hartmann number *Ha*..

and

$$\mathrm{Nu} = \frac{1}{L}\int_0^L \mathrm{Nu}_l dL \tag{23}$$

where h is the convective heat transfer coefficient. The total heat transfer can be significantly influenced by the length of the heated surface wall. For instance, an increase in the length of the heated wall can result in a temperature distribution characterized by small temperature gradients. This, in turn, can lead to a lower Nusselt number *Nu* and, subsequently, a smaller heat transfer coefficient, denoted as *Ncf*. However, despite the associated reduction in heat transfer coefficient, a substantial increase in the surface area could still yield a superior heat transfer rate compared to a scenario with a high Nusselt number but a smaller heated wall length.

Therefore, to facilitate a fair comparison of the total heat transfer rate within the enclosure, it's beneficial to modify the average Nusselt number to reflect the overall heat transfer. This can be achieved by incorporating the non-dimensional length of the heated wall. The modified Nusselt number Nu_m can be represented as:

$$Nu_m = L \times Nu \tag{24}$$

And it can effectively represent the total heat transfer rate in this form. The streamlines in their non-dimensional form are computed using the following:

$$\left(\frac{\partial^2\omega}{\partial X^2} + \frac{\partial^2\omega}{\partial Y^2}\right) = -\left(-\frac{\partial U}{\partial Y} + \frac{\partial V}{\partial X}\right) \tag{25}$$

with the rotational flow ($\omega = 0$) on all surfaces [53,55], and $U = \partial\omega/\partial Y$ and $V = \partial\omega/\partial X$.

3. Numeric technique and model validation

3.1. Finite element numerical method

To solve the fundamental equations, initial conditions, and boundary parameters, the Finite Element Method (FEM) was utilized. This method proved effective for dealing with non-linear sink/source terms resulting from phase changes of NEPCM particles [56,57]. Using a weak form of the main equations and a second-order bifurcation for the heat and momentum equations, the Gauss quadrature integration was implemented at the element level to produce an algebraic system of residual equations. Fig. 2 shows a diagram of solution method. The Newton method was then iteratively applied to solve these equations, and a damping coefficient of 0.85 was introduced to improve convergence [58,59]. In addition, the PARDISO parallel solver was used to facilitate parallel computations across multiple processing units [60,61]. A precision of less than 0.0001 was deemed acceptable for the calculations.

3.2. Element size examination

The effect of mesh resolution on computational accuracy was examined by studying the free convection heat transfer of a NEPCM suspension in a specific test case. The non-dimensional parameters used in the test case were $Ra = 10^5, \theta_f = 0.25, Pr = 6.2, Ste = 0.3, \kappa = 0.33, Nv = 12.5, Nc = 23.8, Ec = 10^{-4}, Ha = 1, L = 0.6$ and $f = 0$, which can be found in the previous studies [2,41,53].

A free-quad form mesh was employed to discretize the solution domain, with the mesh resolution parameter, size number (*Sn*), determining the size of the mesh elements. A small value of *Sn* indicates a fine mesh, while an increase of *Sn* coarsens the mesh. The characteristics of the generated meshes, including the number of elements, as well as the computed average Nusselt number, are presented in Table 3. The local Nusselt number is also depicted in Fig. 3. Additionally, due to the high surface-to-volume ratio of the nanoparticles, the phase transition occurs within a small region of the solution domain. This is visualized through the contours of the heat capacity ratio in Fig. 4, which highlight the regions where phase transitions take place.

Table 3 illustrates a consistent increase in the average Nusselt number as the mesh size parameter (*Sn*) decreases, indicating refinement of the mesh. The table also includes the number of elements for each case. Notably, a 19% increase in mesh elements from 5186 (for $Sn = 0.01125$) to 6400 (for $Sn = 0.01$) exhibits only a 0.4% error compared to a mesh with $Sn = 0.01$, which is deemed acceptable for most engineering applications and visual representation of the results.

In Fig. 3, the local Nusselt number *Nu* is presented for various mesh sizes. It is evident that the curves align well in the central regions of the hot wall. However, at the edges where the fluid changes direction towards the horizontal, a sharp variation in *Nu* can be observed. This discrepancy can be attributed to the sharp edge of the geometry, which

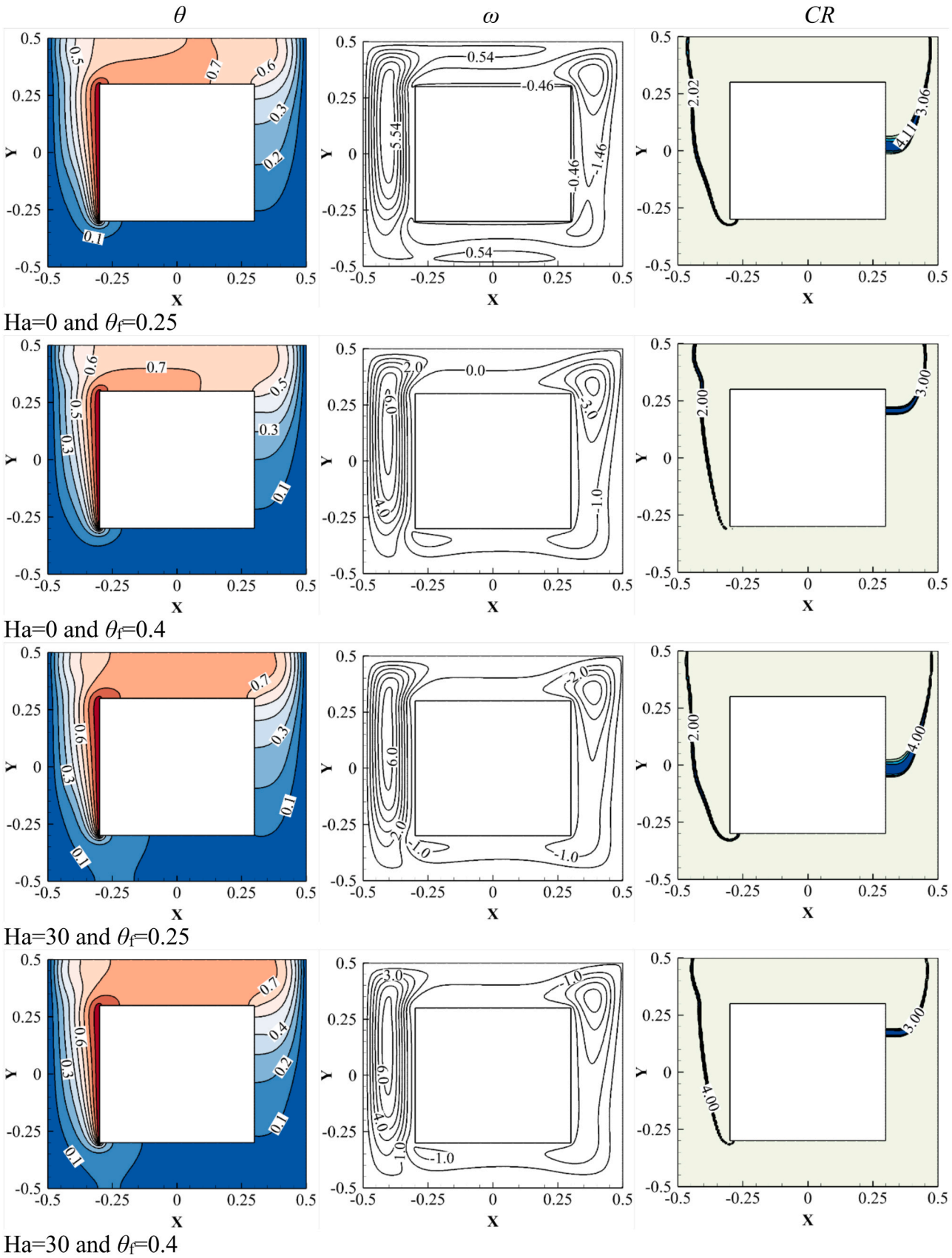

Fig. 13. A comparison of isotherms, streamlines, and CR contours for $Ha = 0$ and $Ha = 30$, $\theta_f = 0, 25$ and $\theta_f = 0.4$ when $Ra = 5 \times 10^5$..

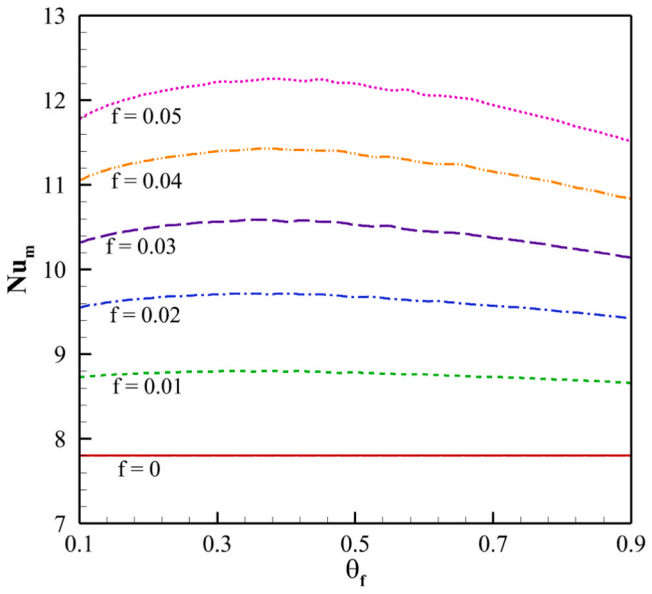

Fig. 14. Variation of the modified Nusselt number as a function of θ_f when $Ra = 5 \times 10^5$..

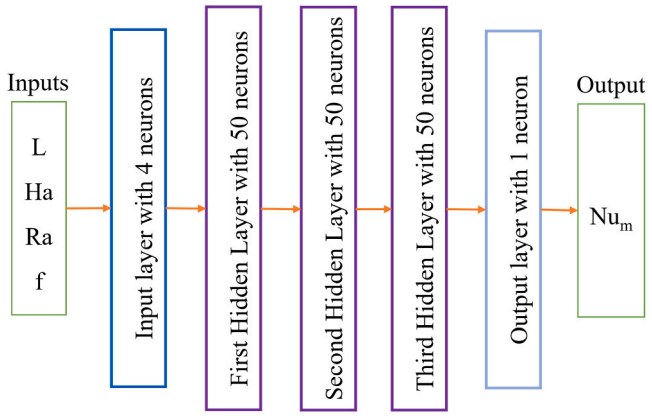

Fig. 15. A schematic view of the utilized NN structure.

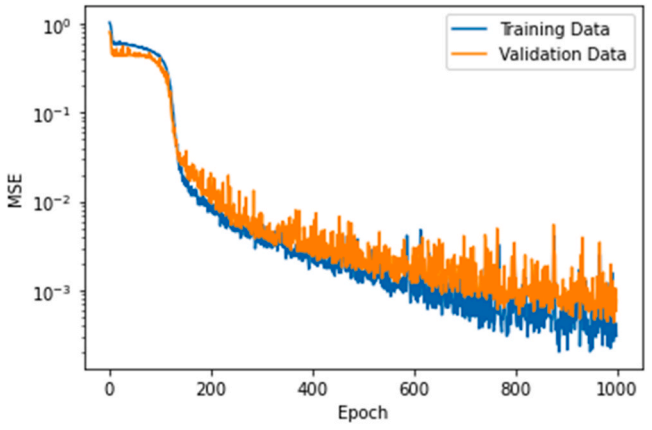

Fig. 16. The training and validation data against Epochs.

can be regarded as an anomaly in the geometry. Further refining the mesh would exacerbate this jump while reducing the surface area. Nevertheless, since these sharp edges are limited to singular points, they

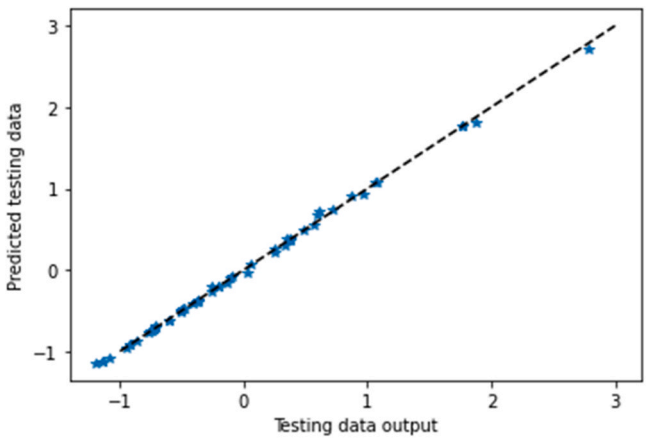

Fig. 17. The predicted test data against the actual test data.

have minimal impact on the average Nusselt number and heat transfer rate.

Fig. 4 showcases the *CR* contours for the finest, coarsest, and intermediate mesh sizes. It confirms that the phase transition through the *CR* field has been accurately captured without any breaks or abnormalities across all meshes. Considering all the graphs and tables, it is evident that the mesh with a mesh number of $Sn = 0.01$ exhibits a uniform structure and converges well. Therefore, the finest mesh with $Sn = 0.01$ was selected to ensure maximum computational accuracy. Fig. 5 depicts a view of utilized mesh.

3.3. Validation of the model

In the pursuit of ensuring the precision of the applied computational code, the investigators drew parallels between their outcomes and the results of two prior scholarly works. Initially, the mean Nusselt numbers derived from the present research were juxtaposed with those documented by Matin and Pop [62]. The focus of Matin and Pop's research was the natural convective flow within an annular space filled with a Cu-water nanofluid. Table 4 showcases the mean Nusselt numbers computed in this study alongside those reported by Matin and Pop [62] for different nanoparticle volume fractions. The comparative analysis reveals a commendable concurrence between the findings of Matin and Pop and the outcomes of this investigation.

Sathiyamoorthy and Chamkha [16] examined magnetohydrodynamic flow and natural convection heat transfer in an enclosure under various heating conditions. The fluid flow was subject to a uniform magnetic field. Here, following formulation of [16], a Hartmann number of $Ha = 50, Ra = 10^5$, and a magnetic angle of 90° was adopted for the sake of comparison, and the results for the temperature field are plotted in Fig. 6. The dots show the results of [16], while the lines depict the current study's results.

4. Results and discussions

In this section, the impact of enclosure aspect ratio ($0.3 < L < 0.9$), Hartmann number ($0 < Ha < 30$), Rayleigh number ($10^3 < Ra < 5 \times 10^5$, fusion temperature for NEPCM particles ($0.1 < \theta_f < 0.9$, and concentration of NEPCM particles ($0 < f < 0.05$) is addressed on the convection heat transfer and the heat transfer rate. The non-dimensional parameters used in this study are consistent with those reported in the mesh examination. Any modifications or changes to the non-dimensional parameters will be explicitly documented and reported.

In their research, Ghalambaz et al. [2] addressed the phenomenon of free convection in NEPCM suspensions contained within a square cavity. The setup involved a hot temperature on the left wall, a cold temperature on the right wall, and insulation on the top and bottom walls. The

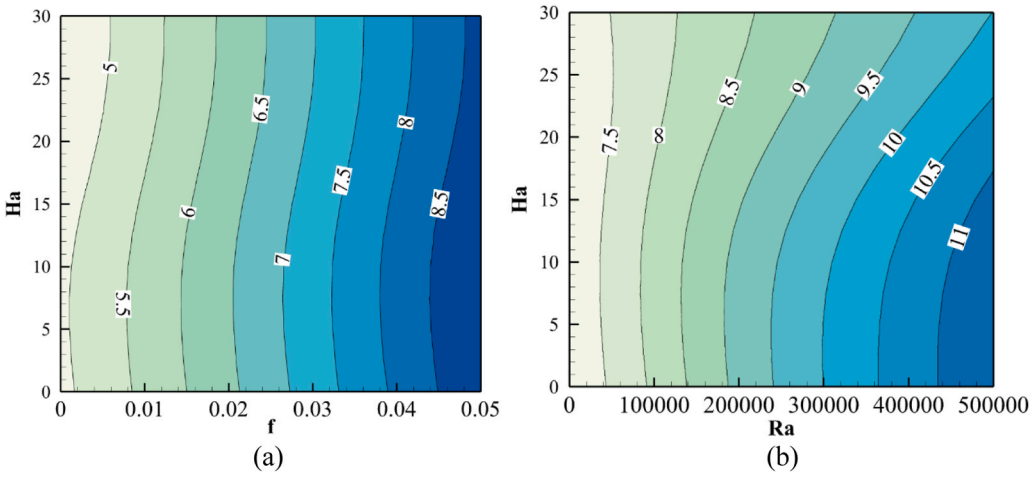

Fig. 18. Estimated values of Nu_m for a range of control parameters (a) Contours of Ha –f and (b) Contours of Ha – Ra..

researchers used *CR* contours, isotherms, and streamlines to illustrate the field variables. A comparison of the current study's findings with those of Ghalambaz et al. [2] is presented in Fig. 7. The comparison reveals a strong correlation between the results of the two investigations, demonstrating the validity of the current study's outcomes.

4.1. Aspect ratio and Rayleigh number

Fig. 8 illustrates the modified Nusselt number (Num) fluctuation with changing Rayleigh numbers across diverse aspect ratios (L). It is observed that at low Rayleigh numbers, the influence of natural convection is not considered substantial, leading to a marginal impact on the rate of heat transfer (Nu_m). However, for Ra around 10^5 and above, an incremental increase in Ra correspondingly amplifies the heat transfer rate (Nu_m). Increasing the aspect ratio enhances Nu_m, as it expands the heat transfer surface area and concurrently diminishes the distance between the warm and cool surfaces, thereby augmenting the temperature gradients adjacent to the heated surface and, in turn, the rate of heat transfer. When the aspect ratio is elevated, $L > 7$, the heat transfer is not significantly affected by the Rayleigh number as the small gap for fluid circulation imposes a resistance to the fluid flow, irrespective of the Rayleigh number strength. In this scenario, the proximity between the warm and cool surfaces precedes determining the temperature gradient and controlling the heat transfer mechanism.

Fig. 9 elucidates the distribution of the local Nusselt number along the heated wall for aspect ratios $L = 0.3$ and $L = 0.7$. At the wall's extremities, the local Rayleigh number is notably high; then, it sharply decays to a constant value towards the center. To investigate this pattern, isotherms, streamlines, and heat capacity ratio (*CR*) contours are plotted in Fig. 10. At the wall edge, the cold fluid moves laterally along the bottom duct before abruptly veering toward the heated wall. This flow dynamic induces a robust local temperature gradient and spikes the local Nusselt number. When the warm fluid departs the heated surface, it must transition towards the top horizontal duct; thus, again, a significant increase in the local Nusselt number is noted. However, the local Nusselt number at the active wall's end is less than at its beginning, which is attributable to the suspension departing the heated surface at an elevated temperature. As a result, the temperature differential at the hot wall's top edge is smaller than at its base. Changes in CR delineate regions experiencing phase transitions. These regions occur around isotherms closely approximating the fusion temperature of NEPCM particles, specifically, $\theta_f = 0.25$. Intriguingly, two sidewalls are at the cooler temperature in this configuration, resulting in two-phase change regions observable in the CR contours. Additionally, with a smaller aspect ratio ($L = 0,3$), there are two dominant flow circulations in the enclosure. One circulation originates from the hot wall, heading towards the left cold wall, and the second from the hot wall towards the adjacent cold wall. This occurs as the gap between the heated and cold walls is adequately large to accommodate double-flow circulation. Nonetheless, as the aspect ratio increases, the gap between the sidewall and hot wall shrinks, permitting only one main flow circulation between the heated and cold wall. With a rise in Rayleigh number, the strength of the free convection flow intensifies, resulting in increased flow velocities and steeper temperature gradients. Hence, as Fig. 10 illustrates, the phase transition regions for CR contours are considerably narrower for Ra= 10^5 compared to Ra= 10^3.

4.2. Fusion temperature and Hartmann number

Fig. 11 elucidates the effect of phase transition temperature and Hartmann number Ha on the modified Nusselt number (Nu_m) when the distance between the hot and cold surfaces is relatively broad, set at $L = 0.6$. Fascinatingly, a peak Nusselt number around a fusion temperature of $\theta_f = 0.4$ is observed across all Hartmann numbers. The Nusselt number diminishes with an increase in Hartmann as the magnetic field introduces a resistive force counteracting the fluid motion, which subsequently dampens the free convection flows and heat transfer.

The local Nusselt number distributions along the hot wall (as shown in Fig. 12) reveal that the magnetic field primarily influences heat transfer around the wall's midpoint. As the Hartmann number escalates, the local Nusselt number near the wall's center decreases. Fig. 13 presents the isotherms, streamlines, and CR contours for two Hartmann numbers: Ha= 0 and Ha= 30. The outcomes are also plotted for two fusion temperatures: θ_f= 0.25 and θ_f= 0.4. Case θ_f= 0.4 was chosen based on the findings from Fig. 11, which depicted a maximum Nu. A rise in fusion temperature shifts the right-side phase transition region upwards, bringing it closer to the heat flow originating from the heated wall. However, alterations in fusion temperature have a negligible impact on the phase transition region on the left side. This can be attributed to the significant temperature gradient existing between the hot and cold surfaces on the left side, resulting in tightly packed isotherms. The distributions of these isotherms are visualized in the isotherm contours and appear dense perpendicular to the hot wall (between the left cold wall and the hot wall). Thus, a change in fusion temperature subtly shifts the region towards the corresponding isotherm.

As discernible in the streamlines, the primary circulation of the suspension occurs in the left region. Comparing the streamlines for Ha= 0 and Ha= 30 shows that the rise in Hartmann number curtails the flow circulation in horizontal ducts and along the hot wall. Nonetheless, the impact of this change is relatively insignificant.

4.3. Fusion temperature and NEPCM concentration

Fig. 14 visually represents the impact of fusion temperature on the heat rate across various concentrations of NEPCM particles. A noteworthy augmentation of the heat transfer rate (Nu_m) accompanies the increase in nanoparticle concentrations.

In a scenario where the nanoparticle concentration $f = 0$, Nu_m remains unaffected by the fusion temperature, as no nanoparticles are engaged in the phase change process. This case could be regarded as a baseline reference for the fluid, devoid of nano-enhancements. As the concentration of nanoparticles escalates, the impact of fusion temperature on heat transfer becomes progressively conspicuous. For instance, with a suspension incorporating a nanoparticle concentration of $f = 0.05$, the highest heat transfer rate is observed around a fusion temperature of $\theta_f = 0.4$. This observation aligns with the results inferred from Fig. 11. Changing the fusion temperature from $\theta_f = 0.1$ (Nu_m=11.8) to $\theta_f = 0.4$ (Nu_m=12.3) results in 4% heat transfer improvement when $f = 0.05$. It should be noted that such an improvement is only due to the change in fusion temperature and does not impact the concentration of nanoparticles or the weight of the suspension. Furthermore, the numerical value for the host fluid's Nu_m ($\varphi = 0$) stands at approximately 7.8. However, with the incorporation of NEPCM particles, this value can be elevated to around 12.6 at $\theta_f = 0.4$. As a result, the utilization of NEPCM particles leads to a substantial improvement in overall heat transfer, increasing it by approximately 38%.

This effect can be rationalized by considering the enhanced thermal properties of NEPCM particles. The addition of nanoparticles can augment the base fluid's effective thermal conductivity and heat capacity, thereby promoting a higher heat transfer rate. Also, during the phase change process, nanoparticles could facilitate uniform heat distribution by mitigating the thermal resistance, leading to an increased heat transfer rate. The fusion temperature affects the phase change process, which is a crucial factor in determining the heat transfer characteristics of NEPCMs. Therefore, by manipulating the fusion temperature and the concentration of NEPCM particles, one can optimize the heat transfer rate for specific cooling applications.

5. Further analysis using neural networks

To further investigate the impact of control parameters on the heat transfer rate, a neural network was employed. The network consisted of three fully connected hidden layers, each comprising 50 neurons with sigmoid activation functions (Fig. 15). The neural network was trained using a dataset of 378 cases, covering a range of parameters as explained in the results section. The input of the neural network included the aspect ratio ($0.3 < L < 0.9$), Hartmann number ($0 < Ha < 30$), Rayleigh number ($10^3 < Ra < 5 \times 10^5$), and concentration of NEPCM particles ($0 < f < 0.05$). The neural network output was the modified Nusselt number (Nu_m).

Prior to training, the records were randomly shuffled, and 70% of the data was used for training, 15% for testing, and 15% for validation. Mean Squared Error (MSE) was chosen as the objective function, and the Adam optimizer [63] was employed. The training process consisted of 1000 episodes with a batch size of 4. The StandardScaler technique was applied to normalize the data. The achieved results include an excellent loss value of 3.65×10^{-4} for training and 3.65×10^{-4} for validation.

Fig. 16 illustrates the progression of MSE error for the train, test, and validation data across different epochs, indicating a consistent reduction as the number of epochs increases. Additionally, Fig. 17 compares the predicted and actual test data, demonstrating a strong model fit. Now that the neural network can accurately predict the effect of the input parameters on the heat transfer rate (Nu_m), it is utilized to generate contour maps illustrating the impact of control parameters.

Fig. 18 (a) and 18 (b) showcase the contour plots of Nu_m for Ha against f and Ha against Ra, respectively. The rest of the parameters were adopted as the default values explained at the beginning of the results section. These contours map the heat transfer rate for a fair range of control parameters. Several thousands of computationally costly simulations were required to produce such a high-resolution map without using the NN approach. Fig. 18 (a) shows that an incline in NEPCM particle concentration (f) increases the heat rate (Nu_m) monotonically; however, an increase in Hartmann number (the magnetic strengths) induces a non-linear impact on the Nu_m. Fig. 18 (b) also shows that an increase in Rayleigh number (Ra) significantly increases the heat rate (Ra), especially at high Rayleigh numbers. Hartmann number primarily impacts the heat rate at high Rayleigh numbers.

6. Conclusions

The primary focus of this research was to address the thermal behavior of NEPCM suspensions in the presence of a non-uniform magnetic field. This study extensively examined the free convection heat transfer within a cavity channel filled with NEPCM particles dispersed in water. The channel was located between two square cylinders and subjected to a non-uniform magnetic field source. The finite element method was applied to solve the governing equations involving the phase change heat transfer. Simulation results were used to investigate the impact of control parameters such as enclosure aspect ratio, Rayleigh number, Hartmann number, fusion temperature for NEPCM particles, and concentration of NEPCM particles on the heat transfer rate (Nu_m). A neural network was also employed to examine further the influence of the control parameters on the heat transfer rate. The neural network was trained using data from multiple scenarios, with inputs including aspect ratio, Rayleigh number, Hartmann number, fusion temperature, and NEPCM particle concentration. The model exhibited high performance in predicting the impact of these parameters on the heat transfer rate. The key findings can be listed as follows:

- It was found that the fusion temperature of NEPCM and Hartmann number Ha have a significant impact on the Nusselt number, particularly when the enclosure aspect ratio $L = 0.6$, with the peak Nusselt number observed at a fusion temperature $\theta_f = 0.4$ across all Hartmann numbers. Notably, an increase in Hartmann number decreased the Nusselt number as the magnetic field imposed a resistive force, dampening the free convection flows and heat transfer.
- The fusion temperature and NEPCM concentration significantly influenced the heat transfer rate. When the nanoparticle concentration $f = 0$ (classical viscous fluid), heat transfer was unaffected by fusion temperature. However, with an increase in nanoparticle concentration, the fusion temperature's impact on heat transfer became more prominent, with the highest heat transfer rate observed around a fusion temperature $\theta_f = 0.4$. A 4% improvement in heat transfer was observed when the fusion temperature was changed from $\theta_f = 0.1$ to $\theta_f = 0.4$ for $f = 0.5$, highlighting the influence of fusion temperature on heat transfer performance. Furthermore, incorporating NEPCM particles results in a significant enhancement of overall heat transfer, yielding an approximate increase of 38%.
- The neural network effectively predicted the impact of input parameters on the heat transfer rate. It was used to generate contour maps to illustrate the effects of control parameters on heat transfer.

Acknowledgments

The authors would like to thank the Deanship of Scientific Research at Umm Al-Qura University for supporting this work by Grant Code: (23UQU4310414DSR009). The work of Ioan Pop has been supported from the Grant PN-III-P4-PCE-2021–0993, UEFISCDI, Romania. Authors wish also to express their thanks to the very competent Reviewers for the valuable comments and suggestions.

References

[1] I. Miroshnichenko, M. Sheremet, Turbulent natural convection heat transfer in rectangular enclosures using experimental and numerical approaches: A review, Renew. Sustain. Energy Rev. 82 (2018) 40–59.

[2] M. Ghalambaz, A.J. Chamkha, D. Wen, Natural convective flow and heat transfer of nano-encapsulated phase change materials (NEPCMs) in a cavity, Int. J. Heat. Mass Transf. 138 (2019) 738–749.

[3] S.U. Choi, J.A. Eastman, Enhancing Thermal Conductivity of Fluids with Nanoparticles, Argonne National Lab.(ANL), Argonne, IL (United States), 1995.

[4] A.I. Alsabery, A.S. Abosinnee, S.K. Al-Hadraawy, M.A. Ismael, M.A. Fteiti, I. Hashim, M. Sheremet, M. Ghalambaz, A.J. Chamkha, Convection heat transfer in enclosures with inner bodies: A review on single and two-phase nanofluid models, Renew. Sustain. Energy Rev. 183 (2023) 113424.

[5] A. Abdulkadhim, I.M. Abed, N. Mahjoub Said, Review of natural convection within various shapes of enclosures, Arab. J. Sci. Eng. 46 (2021) 11543–11586.

[6] V. Tirth, A.A. Pasha, T. Tayebi, A. Dogonchi, K. Irshad, A.J. Chamkha, A. Algahtani, T. Al-Mughanam, A.M. Galal, Magneto double-diffusive free convection inside a C-shaped nanofluid-filled enclosure including heat and solutal source block, Case Stud. Therm. Eng. 45 (2023) 102942.

[7] A.S. Reddy, S. Rajamani, A.J. Chamkha, S. Srinivas, K. Jagadeshkumar, MHD flow of non-Newtonian ferro nanofluid between two vertical porous walls with Cattaneo–Christov heat flux, entropy generation, and time-dependent pressure gradient, Nonlinear Anal.: Model. Control 28 (2023) 1–17.

[8] V. Rajesh, M. Srilatha, A.J. Chamkha, Unsteady Hybrid (Ag–CuO/Water) Nanofluid Flow and Heat Transfer due to a Stretching Sheet with Variable Temperature, J. Nanofluids 12 (3) (2023) 867–876.

[9] D. Chatterjee, N. Biswas, N.K. Manna, D.K. Mandal, A.J. Chamkha, Magneto-nanofluid flow in cylinder-embedded discretely heated-cooled annular thermal systems: Conjugate heat transfer and thermodynamic irreversibility, J. Magn. Magn. Mater. 569 (2023) 170442.

[10] A.A. Mehrizi, F. Besharati, O. Jahanian, H. Hassanzadeh Afrouzi, Numerical investigation of conjugate heat transfer in a microchannel with a hydrophobic surface utilizing nanofluids under a magnetic field, Phys. Fluids 33 (5) (2021).

[11] A.A. Mehrizi, H. Karimi-Maleh, M. Naddafi, F. Karimi, Application of bio-based phase change materials for effective heat management, J. Energy Storage 61 (2023) 106859.

[12] M. Graeilinezhad, H.H. Afrouzi, O. Jahanian, A.A. Mehrizi, Numerical investigation of pseudoplastic fluid flow and heat transfer in a microchannel under velocity slip effect, Eng. Anal. Bound. Elem. 155 (2023) 501–510.

[13] V.R. Hosseini, A.A. Mehrizi, A. Gungor, H.H. Afrouzi, Application of a physics-informed neural network to solve the steady-state Bratu equation arising from solid biofuel combustion theory, Fuel 332 (2023) 125908.

[14] J.H. Merkin, I. Pop, Y.Y. Lok, T. Grosan, Similarity solutions for the boundary layer flow and heat transfer of viscous fluids, nanofluids, porous media, and micropolar fluids, Elsevier, Oxford, UK, 2021.

[15] S. Giwa, M. Sharifpur, M. Ahmadi, J. Meyer, A review of magnetic field influence on natural convection heat transfer performance of nanofluids in square cavities, J. Therm. Anal. Calorim. 145 (2021) 2581–2623.

[16] M. Sathiyamoorthy, A.J. Chamkha, Natural convection flow under magnetic field in a square cavity for uniformly (or) linearly heated adjacent walls, Int. J. Numer. Methods Heat. Fluid Flow. 22 (5) (2012) 677–698.

[17] S.O. Giwa, M. Sharifpur, M.H. Ahmadi, J.P. Meyer, Magnetohydrodynamic convection behaviours of nanofluids in non-square enclosures: a comprehensive review, Math. Methods Appl. Sci. (2020).

[18] P. Patil, S. Benawadi, M.A. Sheremet, The unsteady nonlinear convective flow of a nanofluid due to impulsive motion: Triple diffusion and magnetic effects, Therm. Sci. Eng. Prog. 35 (2022) 101456.

[19] N.B. Khedher, M. Sheremet, A. Saif Alghawli, A. Mohamed, S.A.M. Mehryan, Effect of Non-Identical Magnetic Fields on Thermomagnetic Convective Flow of a Nanoliquid Using Buongiorno's Model, Mathematics 10 (8) (2022) 1222.

[20] C. Sivaraj, S. Gowtham, M. Elango, M. Sheremet, Analysis of thermo-magnetic convection and entropy generation of Al2O3-water nanofluid in a partially heated wavy electronic cabinet, Int. Commun. Heat. Mass Transf. 133 (2022) 105955.

[21] F.L. Rashid, A. Rahbari, R.K. Ibrahem, P. Talebizadehsardari, A. Basem, A. Kaood, H.I. Mohammed, M.H. Abbas, M.A. Al-Obaidi, Review of solidification and melting performance of phase change materials in the presence of magnetic field, rotation, tilt angle, and vibration, J. Energy Storage 67 (2023) 107501.

[22] M.S. Ghoghaei, A. Mahmoudian, O. Mohammadi, M.B. Shafii, H. Jafari Mosleh, M. Zandieh, M.H. Ahmadi, A review on the applications of micro-/nano-encapsulated phase change material slurry in heat transfer and thermal storage systems, J. Therm. Anal. Calorim. 145 (2021) 245–268.

[23] C. Ho, Y.-C. Liu, M. Ghalambaz, W.-M. Yan, Forced convection heat transfer of Nano-Encapsulated Phase Change Material (NEPCM) suspension in a mini-channel heatsink, Int. J. Heat. Mass Transf. 155 (2020) 119858.

[24] J. Mohammadpour, F. Salehi, A. Lee, Performance of nano encapsulated phase change material slurry heat transfer in a microchannel heat sink with dual-circular synthetic jets, Int. J. Heat. Mass Transf. 184 (2022) 122265.

[25] Z. Raizah, A.M. Aly, Double-diffusive convection of a rotating circular cylinder in a porous cavity suspended by nano-encapsulated phase change materials, Case Stud. Therm. Eng. 24 (2021) 100864.

[26] Z. Raizah, A.M. Aly, A rotating superellipse inside a hexagonalshaped cavity suspended by nano-encapsulated phase change materials based on the ISPH method, Int. J. Numer. Methods Heat. Fluid Flow. 32 (3) (2022) 956–977.

[27] A. Sarı, C. Alkan, C. Bilgin, A. Bicer, Preparation, characterization and thermal energy storage properties of micro/nano encapsulated phase change material with acrylic-based polymer, Polym. Sci., Ser. B 60 (2018) 58–68.

[28] J. Shi, X. Wu, R. Sun, B. Ban, J. Li, J. Chen, Nano-encapsulated phase change materials prepared by one-step interfacial polymerization for thermal energy storage, Mater. Chem. Phys. 231 (2019) 244–251.

[29] T. Tayebi, S. El-Sapa, N. Karimi, A.S. Dogonchi, A.J. Chamkha, A.M. Galal, Double-diffusive natural convection with Soret/Dufour effects and energy optimization of Nano-Encapsulated Phase Change Material in a novel form of a wavy-walled I-shaped domain, J. Taiwan Inst. Chem. Eng. (2023) 104873.

[30] S. Hussain, N. Alsedias, A.M. Aly, Natural convection of a water-based suspension containing nano-encapsulated phase change material in a porous grooved cavity, J. Energy Storage 51 (2022) 104589.

[31] M. Sadeghi, A.J. Chamkha, R. Ali, M.B.B. Hamida, M. Ghodrat, A.M. Galal, Hydrothermal behavior of micro-polar Nano-Encapsulated phase change materials (NEPCMs) in an inclined L-shaped cavity, Case Stud. Therm. Eng. 35 (2022) 102039.

[32] S.E. Ahmed, Z.A. Raizah, Analysis of the entropy due to radiative flow of nano–encapsulated phase change materials within inclined porous prismatic enclosures: Finite element simulation, J. Energy Storage 40 (2021) 102719.

[33] A.M. Aly, Z. Raizah, S. El-Sapa, H.F. Oztop, N. Abu-Hamdeh, Thermal diffusion upon magnetic field convection of nano-enhanced phase change materials in a permeable wavy cavity with crescent-shaped partitions, Case Stud. Therm. Eng. 31 (2022) 101855.

[34] E. Golab, S. Goudarzi, H. Kazemi-Varnamkhasti, H. Amigh, F. Ghaemi, D. Baleanu, A. Karimipour, Investigation of the effect of adding nano-encapsulated phase change material to water in natural convection inside a rectangular cavity, J. Energy Storage 40 (2021) 102699.

[35] S. Hussain, Z. Raizah, A.M. Aly, Thermal radiation impact on bioconvection flow of nano-enhanced phase change materials and oxytactic microorganisms inside a vertical wavy porous cavity, Int. Commun. Heat. Mass Transf. 139 (2022) 106454.

[36] A. Alazzam, N.A. Qasem, A. Aissa, M.S. Abid, K. Guedri, O. Younis, Natural convection characteristics of nano-encapsulated phase change materials in a rectangular wavy enclosure with heating element and under an external magnetic field, J. Energy Storage 57 (2023) 106213.

[37] Y. Cao, N. Farouk, H. Ayed, A.A. Aly, F. Jarad, M. Dahari, M. Wae-hayee, B. Saleh, Heat transfer improvement between a pair of heater and cooler inside an energy storage by using nano-encapsulated phase change material/water: A numerical modeling, Case Stud. Therm. Eng. 30 (2022) 101770.

[38] D. Huu-Quan, M. Sheremet, M.S. Kamel, M. Izadi, Investigation of thermal-hydro dynamical behavior on nano-encapsulated PCM suspension: Effect of fin position, fractioning and aspect ratio, Chem. Eng. Process. -Process. Intensif. 157 (2020) 108122.

[39] J. Fereidooni, Heat transfer inspection of nano-encapsulated phase change materials inside a Γ-shaped enclosure influenced by magnetic field, J. Magn. Magn. Mater. 561 (2022) 169682.

[40] W.-R. Liao, L.-H. Chien, M. Ghalambaz, W.-M. Yan, Experimental study of boiling heat transfer in a microchannel with nucleated-shape columnar micro-pin-fins, Int. Commun. Heat. Mass Transf. 108 (2019) 104277.

[41] M. Sheikholeslami, K. Vajravelu, Nanofluid flow and heat transfer in a cavity with variable magnetic field, Appl. Math. Comput. 298 (2017) 272–282.

[42] M. Sheikholeslami, D.D. Ganji, Ferrohydrodynamic and magnetohydrodynamic effects on ferrofluid flow and convective heat transfer, Energy 75 (2014) 400–410.

[43] S. Barlak, O.N. Sara, A. Karaipekli, S. Yapıcı, Thermal conductivity and viscosity of nanofluids having nanoencapsulated phase change material, Nanoscale Microsc. Thermophys. Eng. 20 (2) (2016) 85–96.

[44] M. Sheikholeslami, M. Gorji-Bandpy, D. Ganji, S. Soleimani, Natural convection heat transfer in a cavity with sinusoidal wall filled with CuO–water nanofluid in presence of magnetic field, J. Taiwan Inst. Chem. Eng. 45 (1) (2014) 40–49.

[45] N. Athanasopoulos, A. Baltopoulos, M. Matzakou, A. Vavouliotis, V. Kostopoulos, Electrical conductivity of polyurethane/MWCNT nanocomposite foams, Polym. Compos. 33 (8) (2012) 1302–1312.

[46] M. Ghalambaz, S.M.H. Zadeh, S. Mehryan, I. Pop, D. Wen, Analysis of melting behavior of PCMs in a cavity subject to a non-uniform magnetic field using a moving grid technique, Appl. Math. Model. 77 (2020) 1936–1953.

[47] L. Chai, R. Shaukat, L. Wang, H.S. Wang, A review on heat transfer and hydrodynamic characteristics of nano/microencapsulated phase change slurry (N/MPCS) in mini/microchannel heat sinks, Appl. Therm. Eng. 135 (2018) 334–349.

[48] B. Chen, X. Wang, R. Zeng, Y. Zhang, X. Wang, J. Niu, Y. Li, H. Di, An experimental study of convective heat transfer with microencapsulated phase change material suspension: laminar flow in a circular tube under constant heat flux, Exp. Therm. Fluid Sci. 32 (8) (2008) 1638–1646.

[49] K. Khanafer, K. Vafai, A critical synthesis of thermophysical characteristics of nanofluids, Int. J. Heat. Mass Transf. 54 (19-20) (2011) 4410–4428.

[50] H.R. Seyf, Z. Zhou, H. Ma, Y. Zhang, Three dimensional numerical study of heat-transfer enhancement by nano-encapsulated phase change material slurry in microtube heat sinks with tangential impingement, Int. J. Heat. Mass Transf. 56 (1-2) (2013) 561–573.

[51] A. Zaraki, M. Ghalambaz, A.J. Chamkha, M. Ghalambaz, D. De, Rossi, Theoretical analysis of natural convection boundary layer heat and mass transfer of nanofluids: effects of size, shape and type of nanoparticles, type of base fluid and working temperature, Adv. Powder Technol. 26 (3) (2015) 935–946.

[52] A. Chamkha, A. Doostanidezfuli, E. Izadpanahi, M. Ghalambaz, Phase-change heat transfer of single/hybrid nanoparticles-enhanced phase-change materials over a heated horizontal cylinder confined in a square cavity, Adv. Powder Technol. 28 (2) (2017) 385–397.

[53] S. Mehryan, M. Ghalambaz, L.S. Gargari, A. Hajjar, M. Sheremet, Natural convection flow of a suspension containing nano-encapsulated phase change particles in an eccentric annulus, J. Energy Storage 28 (2020) 101236.
[54] M.A. Sheremet, T. Grosan, I. Pop, Free convection in a square cavity filled with a porous medium saturated by nanofluid using Tiwari and Das' nanofluid model, Transp. Porous Media 106 (2015) 595–610.
[55] A.A. Sakhir Abed, Numerical simulation of laminar incompressible driven cavity flow in a l-shape domain, Int. J. Mech. Eng. Technol. 10 (1) (2019) 119–132.
[56] O.C. Zienkiewicz, R.L. Taylor, P. Nithiarasu. The Finite Element Method for Fluid Dynamics, Seventh edition, Butterworth-Heinemann, Oxford, 2014.
[57] D. Pepper, The Intermediate Finite Element Method: Fluid Flow and Heat Transfer Applications, Routledge, 2017.
[58] C.T. Kelley, Solving Nonlinear Equations with Newton's Method, SIAM, 2003.
[59] P. Deuflhard, Newton Methods for Nonlinear Problems: Affine Invariance and Adaptive Algorithms, Springer Science & Business Media, 2005.
[60] M. Bollhöfer, O. Schenk, R. Janalik, S. Hamm, K. Gullapalli, State-of-the-art sparse direct solvers, Parallel Algorithms Comput. Sci. Eng. (2020) 3–33.
[61] M. Bollhöfer, A. Eftekhari, S. Scheidegger, O. Schenk, Large-scale sparse inverse covariance matrix estimation, SIAM J. Sci. Comput. 41 (1) (2019) A380–A401.
[62] M.H. Matin, I. Pop, Natural convection flow and heat transfer in an eccentric annulus filled by Copper nanofluid, Int. J. Heat. Mass Transf. 61 (2013) 353–364.
[63] I.K.M. Jais, A.R. Ismail, S.Q. Nisa, Adam optimization algorithm for wide and deep neural network, Knowl. Eng. Data Sci. 2 (1) (2019) 41–46.